OEA | Opto-Electronic Advances

Article

April 2026, Vol. 9, No. 4

Open Access

Femtosecond laser maskless direct writing of dual-band crosstalk-free information for all-in-one high-security encryption metasurface

Hanmian Jiang[1], Zhuguo Li[1,2]* and Dongshi Zhang[1]*

Abstract: Metasurface fabrication still faces critical processing challenges in balancing the structural order and disorder, achieving high-speed patterning, and extending material compatibility to refractory metals for operation under extreme conditions. This study demonstrates that femtosecond laser maskless direct writing (fs-LMDW) offers a versatile platform for engineering multispectral information, all-in-one metasurfaces on pure zirconium (Zr) substrates. Through sequential fs-LMDW in air and ethylene glycol (EG), deceptive grey-colored visible information is superimposedly encoded with the infrared (IR)-encrypted information (invisible among black-color structured background), which leverages the crosstalk-free structural modulation of singular-band IR and visible light. The metasurface exhibits robust thermal stability and high-security encryption capability across a wide temperature range, with IR-concealed information (such as QR code) remaining securely encrypted until thermally activated at 300 °C for smartphone-readable information decryption. Furthermore, the visible information is both erasable through 300 °C oxidation heating in air and rewritable via fs-LMDW in EG without compromising IR encryption security. Particularly, the one-time complete erasability makes it possible to identify whether the encrypted IR-information has been decrypted, underscoring the robustness and high security of the platform. The presented hierarchical micro/nanostructuring methodology is deemed to be applicable to a large material matrix to gain high-security, and multifunctional metasurfaces that are more difficult and complex for current metasurface fabrication techniques.

Keywords: all-in-one metasurface; femtosecond laser maskless direct writing; high-security encryption; temperature-controlled decryption; erasability and rewritability

DOI: 10.29026/oea.2026.250303 | CSTR: 32247.14.oea.2026.250303

Citation: Jiang HM, Li ZG, Zhang DS. Femtosecond laser maskless direct writing of dual-band crosstalk-free information for all-in-one high-security encryption metasurface. *Opto-Electron Adv* **9**, 250303 (2026).

1 Introduction

The critical importance of information security in modern life acts as a driving force behind the advancement of cryptography[1]. It fuels the continuous development of robust solutions for digital signatures, secure authentication, anti-counterfeiting, and the safeguarding of sensitive data through encryption. Metasurface has brought us in a new era of multi-channel high-security encryption[2,3], whose optical encryption capacities are flexibly modulable and upgradable through incorporation with external stimuli and responsive materials such as light, heat, and electric fields, and phase change materials (PCMs)[4,5]. Their practical deployment nevertheless remains constrained by the requirement of sophisticated optical decryption systems and displays a pronounced dependence on the high-precision, low-throughput nanofabrication techniques as represented by electron-beam lithography (EBL)[6]. The advent of "quasi-ordered"[7] and "disordered" structural metasurface concepts[8,9] has driven significant breakthroughs in expanding the frontiers of optical encryption and further catalyzes innovations in cost-effective fabrication techniques to lower the lithography's dependency[6,10,11].

Femtosecond laser maskless direct writing (fs-LMDW) has established itself as a transformative platform in metasurface engineering, as distinguished by its unparalleled

Received: 17 September 2025

Accepted: 9 January 2026

Published online: 3 March 2026

[1]Shanghai Key Laboratory of Materials Laser Processing and Modification, School of Materials Science and Engineering, Shanghai Jiao Tong University, Shanghai 200240, China; [2]State Key Lab of Metal Matrix Composites, School of Materials Science and Engineering, Shanghai Jiao Tong University, Shanghai 200240, China.
*Correspondence: ZG Li, E-mail: lizg@sjtu.edu.cn; DS Zhang, E-mail: zhangdongshi@sjtu.edu.cn

capacity for micro-to-nanoscale lithographic patterning capacity[12,13], optical birefringence triggering[11], exceptional structural reconfigurability[14], and extensive material/process compatibilities[15–18]. Its prowess is particularly evident in the high-throughput multifunctionally chemical-physical engineering of plasmonic and hard-to-process materials[15,19], most notable for refractory metals which defy conventional fabrication approaches[20–22]. Full potential to orchestrate an optimal equilibrium among fabrication efficiency, precision, and manufacturability is anticipatable[12,23]. "One stone with two birds" simultaneous creation of laser-induced periodic surface structures (LIPSS) and nanoparticles (NPs) is easily accessible by Fs-LMDW[24,25]. Hierarchical architecture of tungsten LIPSS/NPs has been theoretically established as meta-atoms for visible (Vis) polarization-sensitive chromatic display and multi-band camouflage spanning the infrared (IR) region[20]. By implementing in situ fs laser subtractive/additive integrated manufacturing to yield dimensionally gradient micro/nanostructures, IR-informational encryption and decryption responsive to multiple IR stimuli (e.g., human hand, hot water, cold ice, etc.) while maintaining visual black imperceptibility under ambient conditions have been realized[25].

Despite advancements, multispectral modulation capabilities achieved by fs-LMDW remain substantially underdeveloped compared to those of nanoprinting and other techniques fabricated metasurfaces[2,26]. A critical challenge lies in the hierarchically micro/nanostructuring capacity of fs-LMDW, namely, how to achieve direct writing of both Vis/IR-information in a monolithic metasurface (all-in-one metasurface) to realize non-interferential IR information encryption/decryption display and visual fraudulence (erasable and rewriting of Vis-information would be better). What's more, how to enhance the cryptographic security through selective decryption under harsh environments (e.g., high temperature) as schematically illustrated in Fig. 1, is highly desirable to push the frontier boundary of fs laser fabricated metasurfaces.



Fig. 1 | Schematic concept of fs-LMDW fabricated all-in-one metasurface for integrated visible/infrared information input and crosstalk-free visual fraudulence and IR-encryption/decryption. Thereinto, visible and infrared information is erasable/rewritable and temperature-controlled display, respectively.

In this study, we propose a methodology to monolithically encode both IR/Vis-information on pure zirconium (Zr) refractory-metal substrates without spectral crosstalk, termed as femtosecond laser maskless direct writing (fs-LMDW), which is successively performed in air and ethylene glycol (EG) environments. This approach leverages the environment-dependent physicochemical laser-matter interactions and their excellence in different dimensions of micro/nanostructuing. Hierarchically gradient micro/nanostructures capable of modulating optical properties in the IR-band is achievable in air, while insufficient oxidation featured by abundant oxygen vacancies imparts a black coloration to all products; EG environment exclusively induces oxygen-vacancy-deficient grey-color nanostructuring without any impact on the microstructures corresponding to the pre-encoded IR information. The correlation between fs-LMDW processing parameters and the resultant structural features and the multispectral properties are systematically investigated. Dual-mode information encoding and selective IR-information decryption under high-temperature condition (300 °C) and the accompanied erasability of Vis-information is presented. Fs-LMDW Vis-information rewritability is illustrated with the underlying mechanism being investigated. A simple application scenario is elucidated to exemplify merely one-time complete erasability of the fabricated encryption metasurfaces. The broad material compatibility of fs-LMDW for dual-band spectra modulation is investigated, alongside with a discussion on the possible coloration pathways through oxide and plasmonic material engineering. Finally, the merits of fs-LMDW relative to conventional metasurface fabrication techniques are highlighted, with particular emphasis on its advantages over approaches utilizing PCMs such as $Ge_2Sb_2Te_5$ (GST) and VO_2.

2 Materials and methods

2.1 Meta-unit screening via fs-LMDW in air and liquid

Fs laser ablation of Zr/Mo/TC4-(Ti6Al4V) substrates (dimension: 30 × 30 × 1 mm^3, purchased from Qinghe County Lisheng Metal Materials Co., Ltd.) and W substrates (dimension: 30 × 30 × 0.3 mm^3) was performed using a Trumpf TruMicro 2030 fs laser system operating at a wavelength of 1030 nm, pulse duration of 400 fs, and repetition rate of 400 kHz. Two environments were adopted: air and EG solution. The laser beam was focused onto the sample using an F-theta lens (Linos, 4401-513-00026, f = 167 mm, Germany). A scanning galvanometer system (SCANube III14, SCANLAB GmbH) was used for line-by-line scanning at constant scan speed and scan spacing of 200 mm/s and 5 μm, respectively. Five laser powers of 8, 10, 12, 14, and 16 W were employed to investigate the structural and compositional evolution of the Zr matrix in air and liquid environments. To demonstrate the wide applicability of fs-LMDW to W/Mo/TC4, four powers of 10, 12, 14, and 16 W were adopted. In the liquid-phase condition, each sample was immersed in 15 mL EG within an 80-mm-diameter Petri dish. The liquid thickness between the EG/AIR and EG/sample interfaces was about 2.5 mm. The ablated samples were termed by an environment-power criteria (e.g., AIR 8 W and EG 8 W are indicative of fs-LMDW samples at a laser power of 8 W in air and EG, respectively. After fs-LMDW, all samples underwent two consecutive ultrasonic cleaning in ethanol for 3 minutes to remove the surface residue.

2.2 Sequential fs-LMDW for metasurface fabrication

With respect to the fs-LMDW AIR/EG-hybrid processing for metasurface fabrication, all experimental parameters were kept consistent with the laser power as the variant. IR information is first written on a zirconium substrate (dimensions: 30 × 30 × 1 mm^3) in air, followed by visible information writing in EG environment. The deeply encrypted QR code information of https://www.sjtu.edu.cn is formed through software encoding. It is divided into three parts for stepwise temperature-controlled IR decryption display. First, the background region (non-pattern area) was processed by fs-LMDW at 16 W. Then, laser powers of 12 W, 10 W, and 8 W were sequentially adopted to write three parts of the encrypted QR code. After fs-LMDW in air, the sample was ultrasonically cleaned in anhydrous ethanol and dried by air stream at room temperature. Afterwards, the sample was immersed in EG for visible information encoding by fs-LMDW at a laser power of 10 W. Before information encryption and decryption, the sample was ultrasonically cleaned again in anhydrous ethanol and dried by air flow. To further prove the reconfigurability of the Vis-information erasure by heating treatment at 300 °C and rewriting by fs-LMDW in EG, the deeply encrypted QR code information was fabricated by fs-LMDW in air, followed by the writing-erasure of visible information of "上海" and rewriting of "交通" on the same sample. The cleaning and drying procedures were the same as described above.

2.3 Interface characterizations

Surface morphology and elemental composition were characterized using a field-emission scanning electron microscope (FE-SEM, NOVA NanoSEM 230, FEI) equipped with energy-dispersive X-ray spectroscopy (EDS; Mn Kα excitation at 125.4 eV). Cross-sectional samples were prepared using a focused ion beam (FIB, Helios 5 CX, Thermo Fisher Scientific) and characterized by transmission electron microscopy (TEM, Talos F200X, Thermo Fisher Scientific). With respect to the nanostructures obtained by EG-assisted fs-LMDW, 3D depth and cross-sectional profiles were quantified by atomic force microscope (AFM, MFP-3D, Oxford Instruments), while the hierarchical micro/nanostructures

obtained in air were assessed by a confocal laser scanning microscopy (CLSM, VK-X3000, KEYENCE). Reflective spectra spanning from UV to NIR band and in the MIR band were measured using UV-Vis-NIR spectroscopy (Lambda 950, PerkinElmer) and Fourier-transform infrared spectroscopy (FT-IR; Nicolet 6700, Thermo Fisher Scientific), respectively. Chemical state analysis was performed using multiple complementary techniques: Raman spectroscopy (Senterra R200-L, Bruker Optics) with 532 nm excitation was employed to identify molecular vibrations; X-ray diffraction (XRD, Aeris, Malvern PANalytical) using Cu Kα radiation (λ = 0.15419 nm) was utilized to determine crystallographic phases; and X-ray photoelectron spectroscopy (XPS; AXIS UltraDLD, Kratos Analytical) with monochromatic Al Kα source was applied to analyze surface chemistry and electron paramagnetic resonance (EPR; EMXplus, Bruker BioSpin) was used to complement these measurements through the detection of defect states. Additionally, infrared temperatures and images of the sample surface were measured by a thermal infrared camera (FLIR, E60) to visualize the IR encryption information.

3 Results and discussion

To systematically screen the meta-unit for fabricating all-in-one metasurfaces, fs-LMDW of Zr plates was respectively conducted in air and EG environments. Figure 2(a, b) presents the morphological characteristics and 3D depth profiles of the resulting structures with detailed characterizations shown in Fig. S1. When fs-LMDW processed in air at the laser power of 8 W, hierarchical micro/nanostructures are produced: laser-induced periodic surface structure (LIPSS) is located at the base which is overlaid by nanoparticles (NPs) aggregates. The driving forces include the yield of high-pressure and high temperature (HPHT) extreme environments, along with the yield of surface plasmon polaritons (SPPs), laser induced shockwave and NPs self-assembly[27]. Elevating the laser power to 12 W leads to a moderate increase in the density and height of NPs aggregates, partially obscuring the underlying LIPSS, while further increasing the laser power to 16 W promotes the development of microspikes comprehensively covered by particulate deposits (Fig. 2(a), upper part).

The presence of submicron-scale particles indicates the occurrence of intense laser thermal ablationl[28]. Other dynamics such as rapid solidification[29] and convective mass transport[30] are instrumental in spike-structure formation. This phenomenon has been previously reported on stainless steel[31], silicon (Si)[30], and titanium (Ti)[32]. The structural evolution is corroborated by quantitative measurements of surface roughness, which increases from 1.03 μm to 4.23 μm as laser power rises from 8 W to 16 W (Fig. 2(c), left). In contrast, fs-LMDW in EG yields hierarchical nanostructures characterized by coexistent low-spatial-frequency LIPSS (LSFL) and ultrahigh-spatial-frequency LIPSS (UHSFL), (Fig. 2(a), lower part) whose formation is attributable to the material melting[33] and interfacially Marangoni-driven bursting behavior[34]. Increasing the laser power from 8 W to 16 W induces the pronounced structural inhomogeneity within the LSFL/UHSFL matrix, resulting from enhanced thermal effect and longer melting lifetime, more turbulent particles ejections and ultrafast solidification owing to the high quenching rate[35], and more complex bubble dynamics[36] and laser–bubble interactions[37]. Despite morphological variations, surface roughness remains consistently confined within 60 ± 10 nm (Fig. 2(c), right), indicating fs-LMDW in EG environment is advantageous for LIPSS-correlated nanomanufacturing.

XRD analysis (Fig. 2(d)) reveals a pronounced fs-LMDW atmosphere-dependent oxidation behavior. A distinct phase transition from metallic Zr to monoclinic (m-ZrO_2) and tetragonal (t-ZrO_2) zirconia is observed after air-fs-LMDW at 8 W, whereas only the pure Zr phase is detected in the EG environment. This discrepancy is attributed to the significant attenuation of pulse energy during laser propagation in liquid medium[39], consistently in comparative studies of NPs synthesis via laser ablation in air and liquids[40]. Increasing the laser power to 16 W remarkedly enhances the oxidation kinetics, intensifying the characteristic signatures of m- and t-ZrO_2 phases. This trend is particularly evident in air, as further corroborated by Raman spectroscopy characterization (Fig. 2(e)), with the vibrational modes of t-ZrO_2 at 149/260/327 cm^{-1}, and m-ZrO_2 at 181/372/468/557/634 cm^{-1} [41,42]. The Raman spectra of structures obtained in EG are featureless, with several broad peaks seemingly related to t-ZrO_2 and m-ZrO_2 phases (Fig. S2), indicating the LIPSS structures are highly possible in the metal-dominant, amorphous or quasi-crystal state formed by surface melting and solidification[33,43].

Both air and organic-solvent environments can induce metal oxidation upon fs laser irradiation[25,44], while the latter can also promote metal carbonization[34] and carbon deposition[34,39]. Consistent with these reports, our EDS, Raman, and XPS analyses (Fig. 2(f–h)) confirm the carbon incorporation in the EG-processed samples. EDS quantitative results indicate substantially higher carbon contents in structures formed in EG than those formed in air (Fig. 2(f)). Raman spectra further affirm selective carbon formation in EG, exhibiting characteristic D and G bands within 1300–1400 cm^{-1} and 1550–1600 cm^{-1}, respectively (Fig. 2(g)). The intensity ratio I_D/I_G exceeds 2.0, indicating a higher degree of structural disorder[45]. Such elevated ratios (>1) indicate the predominant formation of structurally disordered amorphous carbon (a-C) domains[46]. XPS C1S analysis identifies a distinct Zr–C bond at a binding energy of 281.80 eV exclusively in the EG-sample (Fig. 2(h)), while XPS Zr 3d spectra demonstrate that EG-LIPSS has a higher percentage of pure Zr phase than particles-aggregates formed in air (Fig. 2(i)). According to the temperature-dependent phase transition sequence of cubic ZrO_2 (c-ZrO_2) > t-ZrO_2 > m-ZrO_2[38], it is

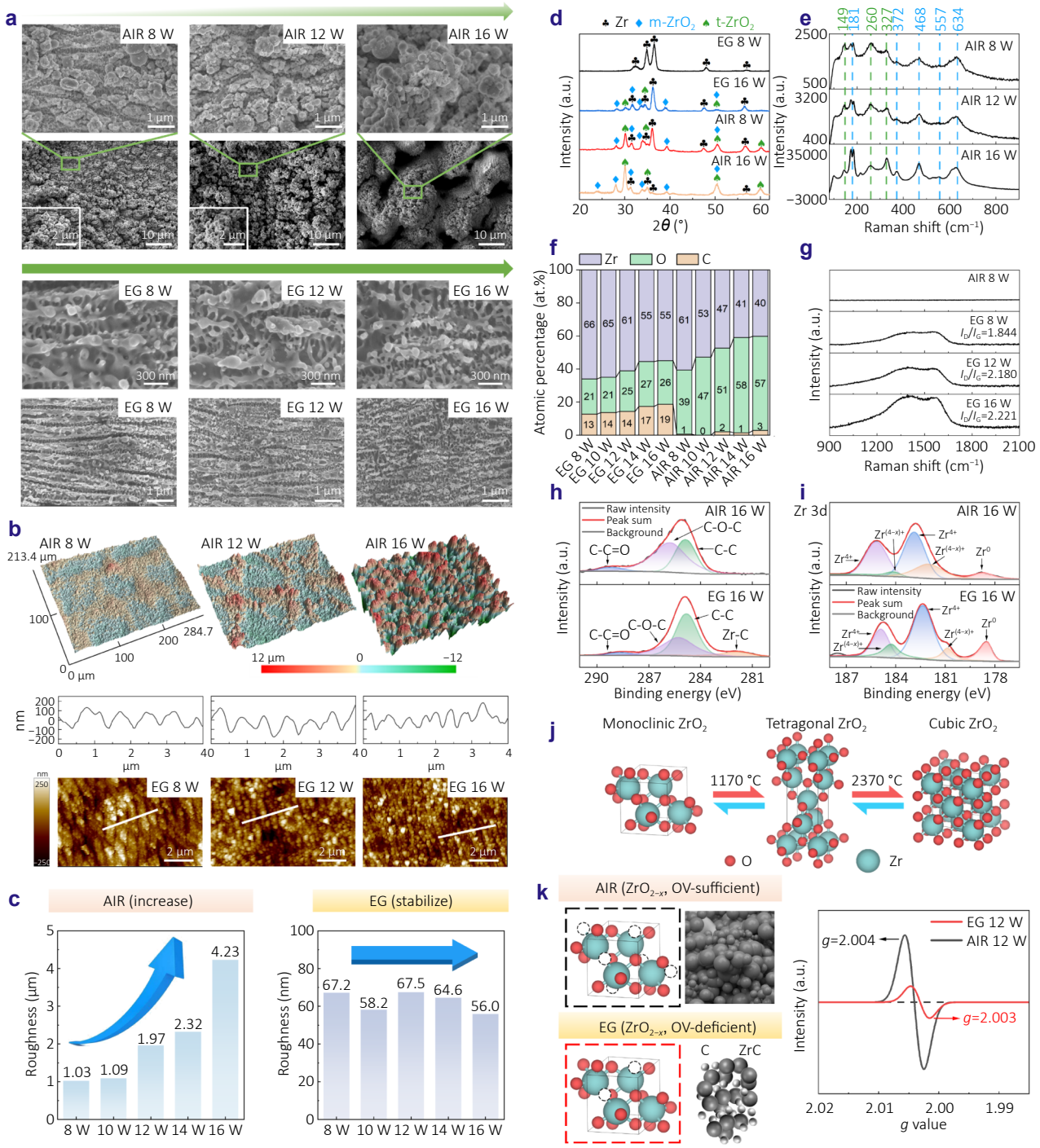


Fig. 2 | Structural and compositional analysis of fs-LMDW in AIR and EG environments. (a) Low/high-magnification SEM images of resultant surface structures obtained by fs-LMDW in air and EG environments at laser powers of 8 W, 12 W and 16 W. Details of structures are shown in Fig. S1. (b, c) 3D topography and roughness summary of AIR/EG-assisted fs-LMDW samples, respectively. (d) XRD spectra of EG 8 W, EG 16 W, AIR 8 W and AIR 16 W samples and marking of associated Zr (PDF#04-008-1477), m-ZrO_2 (PDF#04-001-7279), and t-ZrO_2 (PDF#01-070-7300) phases. (e–g) Raman spectra of AIR-assisted fs-LMDW, EDS elemental (Zr/O/C) atom-percentages of all as-prepared samples, and Raman spectra of carbon featured peaks for AIR/EG-assisted fs-LMDW samples. (h, i) High-resolution C 1s and Zr 3d XPS spectra of AIR 16 W and EG 16 W samples. (j) Temperature-correlated phase transition from monoclinic ZrO_2 to tetragonal ZrO_2 and cubic ZrO_2. (k) Schematic illustration of morphological and compositional differences of obtained structures in air and EG environments and corresponding EPR spectra demonstrating the sufficient/deficient density of oxygen vacancies (OV) within ZrO_{2-x}. Figure reproduced from: (j) ref[38], Elsevier Ltd.

inferred that the local temperature induced by fs-LMDW exceeds 1170 °C (Fig. 2(j)). The dominance of the metastable t-ZrO_2 phase underscores the characteristic ultrafast heating and quenching rates intrinsic to fs-LMDW at a magnitude of 10^{12}–10^{14} K/s[47–49]. Nanoscale structuring may also contributes to an increased surface energy, promoting size-dependent thermodynamic stabilization of t-ZrO_2 phase[50].

When fs-LMDW is performed in organic solvent, the synthesized nanomaterials are dispersed in the liquid medium[51]. Consequently, the resulting surface structures primarily comprise hierarchical LIPSS nanostructures with minimal particulate deposition (Fig. 2(k)). In contrast, fs-LMDW in air leads to substantial redeposition of NPs, which accumulate densely on the surface to form particulate aggregates, acting as fundamental building blocks for both structural and optical modulation[24,25]. EPR analysis (Fig. 2(k)) demonstrates a higher density signal of oxygen vacancies (g=2.004) for structures obtained in air. This is due to the dominant oxidation reaction pathway[25], Gaussian-beam-induced gradient oxidative ablation[52], laser defect engineering[53] and non-equilibrium dynamics during particle synthesis[54], which collectively favoring the formation of nonstoichiometric oxides[25,55].

Oxygen-vacancy-rich non-stoichiometric ZrO_{2-x} structures prepared by fs-LMDW in air are excellent black absorbers with low visible-reflectance and modulable MIR-reflectance (Fig. 3(a, c)), supporting the flexibility and ease of fs-LMDW to fabricate black absorbers and emitters[56]. In contrast, the hierarchical LIPSS nanostructures produced in EG exhibit slightly higher visible reflectance (Fig. 3(b, e)), attributable to the lower density of oxygen vacancies (Fig. 2(k)) and a higher percentage of pure Zr (Fig. 2(i)). Theoretical color values derived from reflectance spectra are converted into CIE XYZ, CIE L*a*b, and HSL color space coordinates, as summarized in Fig. S3, confirming minimal chromatic deviation among air-ablated samples. Increasing the laser power from 8 W to 16 W for fs-LMDW in air results in the reflectance reduction of MIR band in the wavelength range of 8-13 μm (LWIR, Long Wavelength Infrared) from 30.1% to 20.9% (Fig. 3(c)), about 9.2% enhancement of IR emissivity (emissivity = 1 – reflectance), whereas the visible-band reflectance is relatively stable, insensitive to the laser power alteration. Due to the absence of microstructures, the overall MIR-reflectance of EG-structures is much higher (Fig. 3(b, e)). The AIR/EG-structures display distinct saturation and lightness profiles (Fig. 3(d, f)) because of the black and (brown) grey appearance. Within each series, the values of color saturation and lightness are very close, indicating the large processing window for similar-color alteration and information encryption[25].

According to the Stefan-Boltzmann law ($E = \sigma\varepsilon T^4$), the infrared radiation energy (E) is proportional to the emissivity (ε) and the fourth power of absolute temperature (T)[57]. Under elevated temperatures, the resultant radiative emission is substantially amplified, suggesting that the interfacial temperature with high emissivity is comparatively higher in a thermal camera[25,58]. Our experimental results reveal the same trend when heating the samples from 50 °C to 300 °C (Fig. 3(g, h)). The temperatures of air-specimens significantly exceed those of EG-counterparts under the same conditions. A clear decreasing trend of the maximal temperature difference (ΔT) between the surface temperature and the setting heating temperature is observed (cross arrow) for air-samples processed at higher laser powers with higher emissivities (Fig. 3(g), left); whereas EG-ablated samples exhibit a minimal temperature variation under the consistent heating conditions (Fig. 3(h), left). Figure 3(i, j) summarizes the morphological and spectral properties of structures obtained in air and EG environments, respectively. The low reflectance difference of the black absorbers (hierarchical micro/nanostructures) formed in air can easily endow imperceptible encoding of black-color information but sensitive to the increase of samples' temperatures, while the LIPSS nanostructures generated in EG exhibit highly consistent spectral properties in the LWIR atmospheric window but display different colors in the visible band as compared that of air-assisted fabricated specimens. In light of their separated visible/infrared-band spectra modulation capacities, they are deemed to be good partners to develop novel metasurfaces as conceptionally proposed in Fig. 1 for visual discrimination by the human eye (EG-fs-LMDW), with air-fs-LMDW-encoded IR-information in the underlying structures being resistent to the rewritable EG-fs-LMDW nanomanufacturing and composition alteration upon high-temperature thermal treatment.

All-in-one metasurface supporting dual-band information crosstalk-free display is fabricated as schematically in Fig. 4(a), simultaneously integrating visible "SJTU" pattern and an QR code IR-information on a Zr substrate (3 cm × 3 cm × 1 mm). A thermal "lock" is set as the "key" for high-security IR-information decryption, requiring the substrate's temperature to be elevated to 300 °C for full information retrieval (Fig. 4(b)). The IR-band QR code is fabricated by air-fs-LMDW through gradient laser structuring at laser powers of 8 W, 10 W, and 12 W, while the background is processed at 16 W. The uniform visual black appearance across the whole region effectively conceals the underlying IR information, providing visual encryption. Subsequently, deceptive grey color visible information is inscribed via fs-LMDW in the EG environment, yet their thermal properties remain close to the background, ensuring no interference with the encrypted IR-band QR code. At ambient temperature (16 °C, winter), the IR information remains fully encrypted. Partial decryption occurs upon heating to 50 °C and 100 °C, with complete decoding achieved at 300 °C, where the QR code becomes readable using a standard smartphone (Fig. 4(c–e)). Concurrently, the visible "SJTU" pattern is thermally erased. The encrypted QR code is highly stable after twenty-cycles of IR-encryption/decryption tests between room temperature and stimuli heated at 300 °C (Fig. S5).

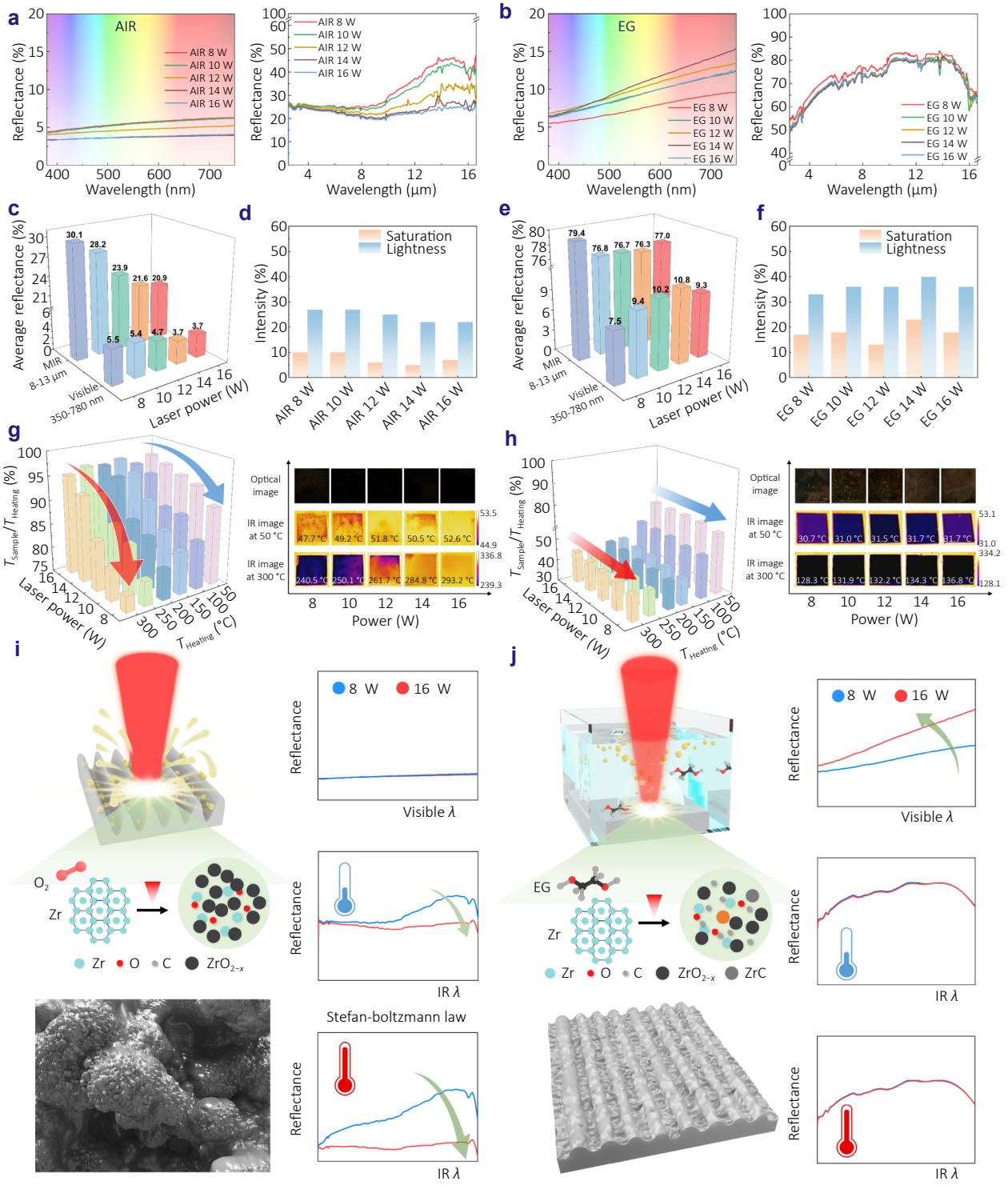


Fig. 3 | Optical and thermal properties. (a–f) UV-Vis, MIR reflectance spectra, average reflectance and color saturation/lightness statistics of samples obtained by fs-LMDW in air and EG, respectively. (g, h) Thermal evolution trend ($T_{Sample}/T_{Heating}$) for AIR/EG-samples obtained at laser powers of 8, 10, 12, 14, and 16 W upon heating at temperatures of 50, 100, 150, 200, 250 and 300 °C and corresponding optical and IR images at 50 °C and 300 °C. (i, j) Schematic illustration of structural, compositional, and optical regulation capacities by reactive fs-LMDW in air and EG environments, respectively.

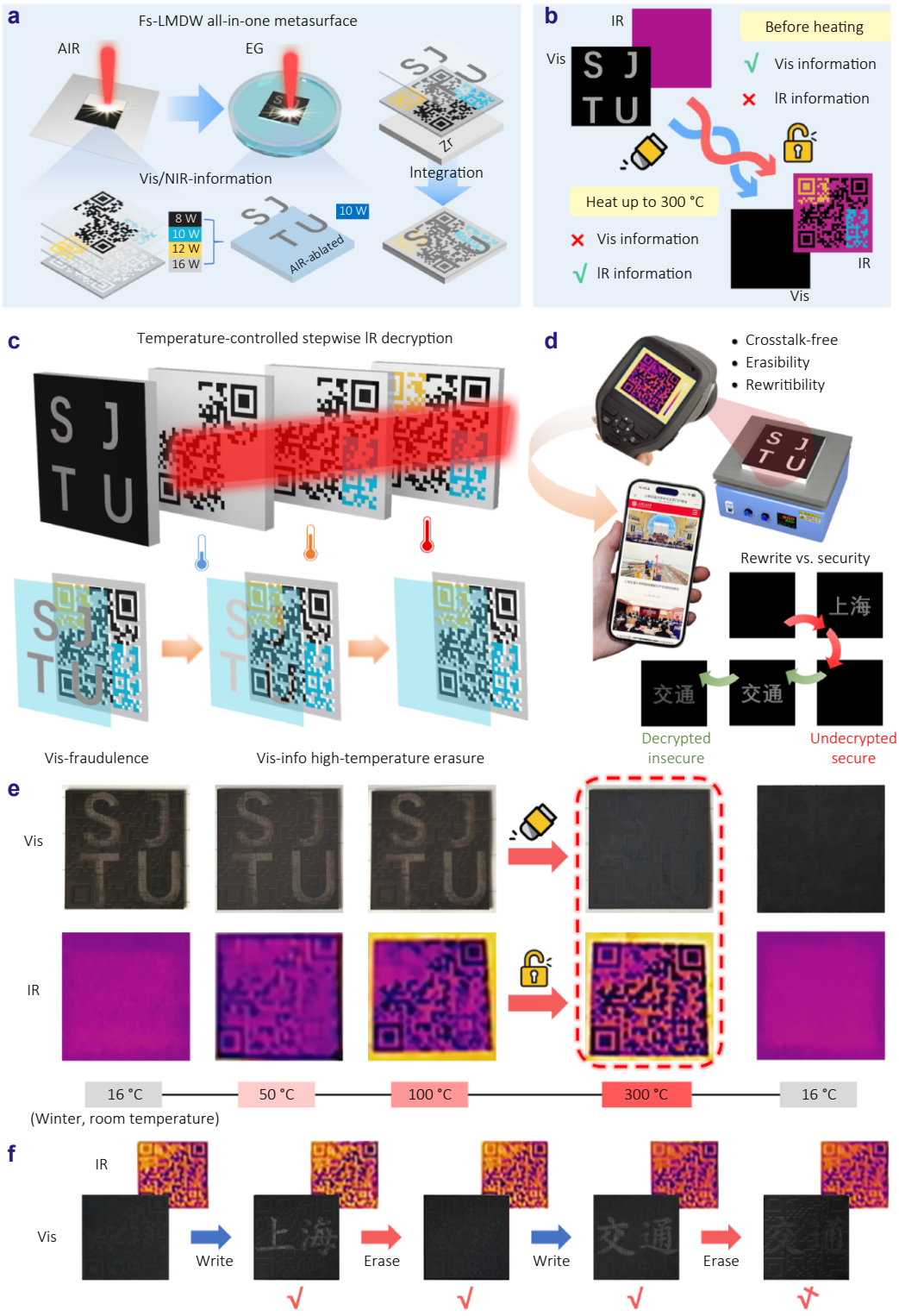


Fig. 4 | All-in-one crosstalk-free metasurface fabrication by fs-LMDW and advanced high-security encryption and decryption. (a) Fabrication flow of sequential fs-LMDW in air and EG environments to encode infrared and visible information. (b) Scheme of crosstalk-free information modulation capacity in Vis/IR bands. (c) Schematic illustration of thermal-driven stepwise IR-information decryption, Vis-information erasure and final disappearance of Vis-information and display of complete QR code information. (d) Scheme of website decrypted by scanning IR-band QR code by a cellphone at 300 °C, erasability and rewritability and the relationship between the Vis-display performance and the security of encrypted information. Additional snapshots for visible information erasability at temperatures at 200 °C and 280 °C are shown in Fig. S4. (e) Visible (top) and IR (bottom) images at increased temperatures from room temperature (16 °C) to 300 °C. (f) Erasable "上海" and rewritable "交通" visible information and corresponding IR images of the steadily encrypted QR code.

We further demonstrate sequential writing, erasure, and rewriting of visible content ("上海" followed by "交通") on the same QR-code IR-encoding substrate (Fig. 4(d, f)). The first erasure cycle completely removes all visible information, whereas residual information marks are observable after the 2nd erasure process. It can help to check whether the IR information has been decrypted after heating the sample at 300 °C. If it is completely erasable, it means that this sample has not been subjected to high temperature IR decryption and fs-LMDW rewriting in EG, while if impossible to completely erase the visible-information, it means that someone has already decrypted the encrypted IR-information and it is no longer safe.

To elucidate the underlying erasure mechanism, a detailed investigation of the morphological and compositional evolution at the Vis-information interface boundary was conducted before and after heating treatment at 300 °C. As illustrated in Fig. 5(a), both the AIR-fs-LMDW and the EG/AIR overlapping zones (designated as AE) exhibit negligible morphological alteration following 300 °C heating. The EG-fs-LMDW patterning on the AIR-fs-LMDW QR-coding region (composed of LIPSS and NPs-aggregates) effectively removes the particulate, leading to a reduction in the surface roughness (Fig. 5(b), upper). Both configurations remain structurally stable against 300 °C heating treatment (Fig. 5(b), lower). Raman spectroscopy (Fig. 5(c)) confirms the retention of carbon within the EG-patterned structures, as evidenced by the persistent D and G bands and ZrO_2 is detected within all samples. EDS analysis further reveals an increase in oxygen content within both regions after heating, with the compositional discrepancy between the AIR and AE zones decreasing from 7% to 2% (Fig. 5(d)), signifying the occurrence of homogeneous oxidation during 300 °C annealing. This finding is substantiated by cross-sectional profiling (Fig. 5(e)), which identifies a distinct oxide layer approximately 100 nm thick, absent in the pristine Zr-LIPSS sample. High-resolution TEM (HRTEM) coupled with fast Fourier transform (FFT) analysis delineates a multilayered architecture: the outermost surface is an amorphous zone (State I), several to tens of nanometers in thickness, which is underlain by the layer of hexagonal Zr oriented in different crystalline directions (States II and III), in consistent with LIPSS formation mechanism via transient melting and rapid solidification[33]. After thermal treatment, LIPSS surface undergoes oxidation transformation into a graded structure comprising an amorphous and t-$ZrO_{1.98}$ layer atop the Zr substrate. The erasability of visible information also benefits from the high thermal stability of black non-stoichiometric zirconia (ZrO_{2-x})[59] which is the composition of structures responsible for the steadily displayed encoded IR information. EG-fs-LMDW should induce a reductive reaction of metallic Zr, which undergoes incomplete oxidation during thermal heating at 300 °C[60] to blacken the surface, realizing visible-information erasure. Note that there is a laser-power threshold for the visible-information erasability and crosstalk-free dual-band information display, as indicated in Fig. S6. Visible information is erasable and rewritable less than 14 W, but can no longer be erased at 14 W due to hierarchically oxidative structuring which significantly influences the encrypted IR information structures.

The present work exhibits limited visible-color diversity within the Zr-ZrO_x material matrix. Therefore, assessing the wide mateiral applicability of fs-LMDW and enhancing coloration capacity of fabricated metasurfaces become two important issues. We applied fs-LMDW to Mo, W, and Ti_6Al_4V (TC4) in air and EG, respectively. UV-NIR to MIR reflection spectra (Fig. 6(a)) show material-dependent spectral control despite similar visible colors. Air-processed samples all appear black (<10% reflectivity), but MIR modulation varies significantly: Mo > W > TC4, inversely correlating with their melting points (Mo: 2620 °C, W: 3422 °C, TC4: 1670 °C). Notably, Mo samples exhibit greater MIR modulation than Zr samples (Fig. 6(b)), despite lower structure height. This result is analogous to the gradient hierarchical WO_{3-x} micro/nanostructures obtained by fs laser ablation of W in the quartz-confined space[25], indicating the large structural/spectra modulation window is enabled by seemingly disordered but in reality relatively homogeneous particles' deposition and aggregations. The MIR modulation capacity, however, diminishes markedly for both W and TC4, inversely correlating with their respective high and low melting points. The limited fs-LMDW modulation for W is principally due to its arduous processability and reduced yield of particles for the formation of gradient microstructures[20]. For TC4, its considerably lower melting point promotes facile fs-laser ablation, leading to rapid saturation of the hierarchical micro/nanostructure development and thus constrained modulation. Processing in EG liquid environment, conversely, leads to the near-identical MIR reflectance spectra for fs-LMDW Mo/W samples but disparate visible colors, analogous to Zr samples processed under similar conditions. This spectral decoupling underscores their applicability in fs-LMDW-based, crosstalk-free Vis/IR information encryption. Critically, their enhanced thermal stability (melting points exceeding Zr (1852 °C)[61] further potentiates high-temperature encryption capabilities.

Given the well-established prowess of fs lasers in functional micro/nanostructuring, fs-LMDW technique demonstrably extends to numerous transition metals (Fig. 6(c)), with potential applicability broadening to semiconductors and diverse material matrices. While TC4 exhibits significant spectral deviations in both visible and infrared bands under current parameters, this preliminary result does not preclude its viability; rather, it necessitates optimization of the processing window. Fs-LMDW is often accompanied by the yield of high-density oxide particles and their in situ deposition into aerogels[24]. The density of deposited aerogel is controllable via equipping a dust collector and changing scan intervals[27], while composition and visible coloration are tunable through selection of fs-LMDW target materials.

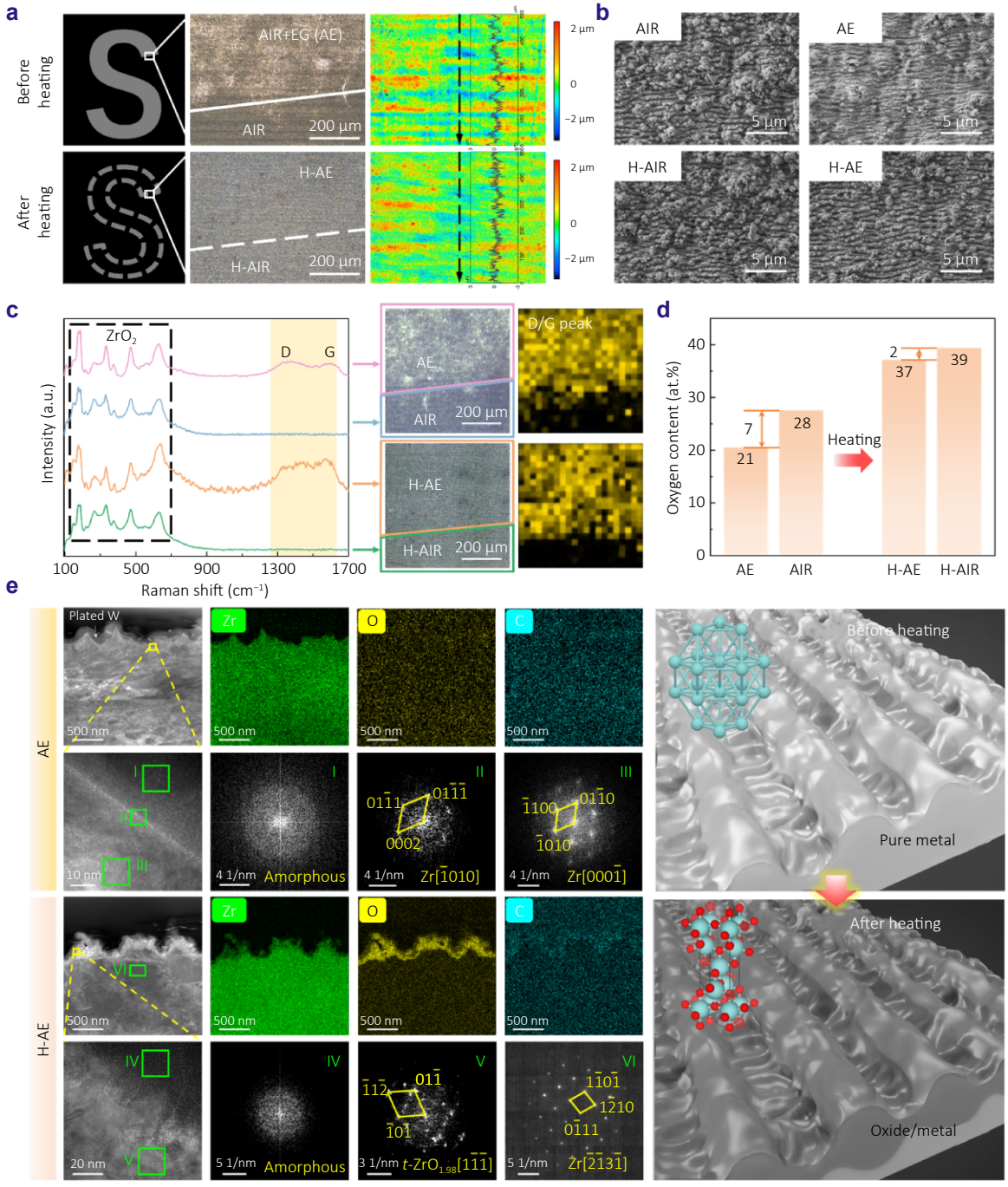


Fig. 5 | Mechanism analysis of visible information erasability. (a) Optical and confocal profile images of the erased Vis-information region before and after heating at 300 °C. (AE: AIR zone reprocessed by fs-LMDW in EG; H-AE: AE zone after heating; H-AIR: AIR zone after heating). (b–d) SEM images, Raman spectra, carbon mapping and EDS atomic oxygen percentage of AE, AIR, H-AE and H-AIR zones. (e) TEM/EDS and HRTEM/SAED analysis of cross-sectional AE and H-AE zones and corresponding schematic of structural layouts and phases before and after 300 °C heating treatment.

Vibrant multi-coloration should be achieved through interfacial particle disposition and nanoscale sintering, minimally impacting the underlying IR-encrypted microstructures. Leveraging the broad material compatibility is achievable by fs-laser nanomaterial synthesis[51,63] and high-resolution laser forward printing[64,65]. Further color enrichment should be also feasible via interfacial plasmonic metal particles (e.g., Ag, Au), enhancing visible display without compromising high-security IR decryption. The resulting all-in-one metasurfaces exhibit performances comparable to, and in aspects advantageous over, state-of-the-art lithography-based counterparts[66] and other alternative crosstalk-free

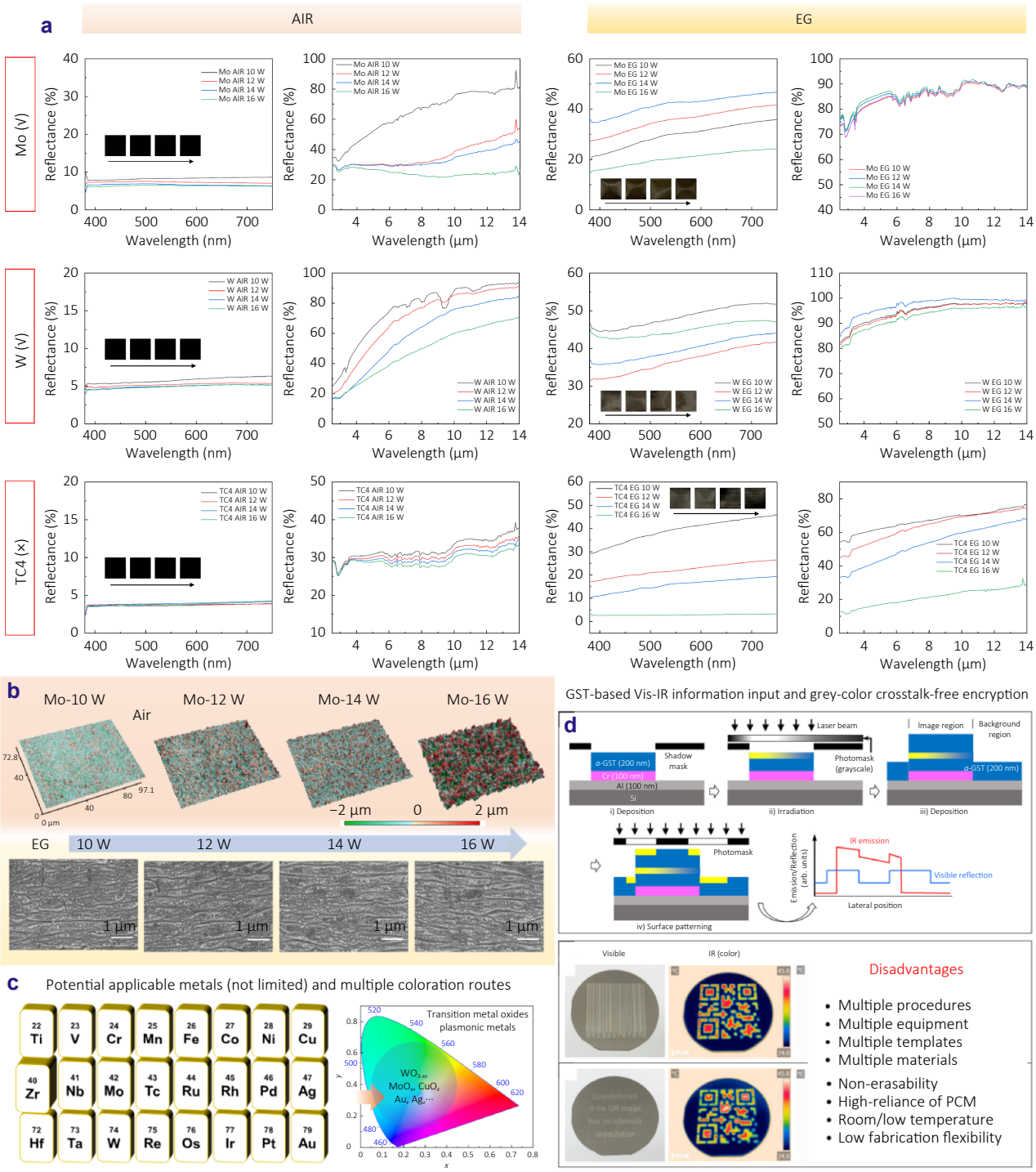


Fig. 6 | Multiple-material exploration, potential applicable material matrix and coloration routes, and comparatively disadvantages of multi-layer GST encryption technique. (a) UV-NIR and MIR refection spectra of Mo/W/TC4 samples fabricated by fs-LMDW in air and EG environments, respectively, and the corresponding optical images (inset). (b) Confocal 3D profiles and SEM images of fs-LMDW fabricated Mo samples obtained at 10, 12, 14 and 16 W, respectively. (c) Potential applicable metals (not limited) and multiple coloration routes. (d) Scheme for fabrication of multi-layer visible/IR-information crosstalk-free GST metasurface and corresponding Vis/IR-band display performances, and the summarized comparatively disadvantages from fabrication, display and material perspectives. Adaptively printed from ref.[62], Copyright 2022 Wiley-VCH GmbH.

cryptographic systems, such as hybrid planar plasmonic cavities[67], mask-guided multilayer deposition and structuring[62,68,69], as detailed in Table 1.

Contemporary thermal emissivity encryption/decryption is predominantly exploited through the semiconductor-to-metal transition in VO_2[68,70] and the amorphous-crystalline (a-c) phase transition in $Ge_2Sb_2Te_5$ (GST)[62]. GST-based encryption systems inherently lack gradual decryption capability unless crystallization gradients are precisely engineered. Erasing visible-information in the form of c-GST mandates energy-intensive reamorphization via ultrafast quenching such as laser irradiation[74]. GST's chromogenic output is restricted to grayscale unless altered by selectively patterned coating of IR-transparent materials (e.g., Si, Si_3N_4, Si_3N_4/Ge, TiO_2) with the assistance of preprepared pattern masks[68,72]. When c-GST is adopted as the underlying IR-information module, erasure is accessible by annealing at 150 °C via c-to-a-GST phase transition[71,72]. While W-doped VO_2[73,75] enables tunable thermal emission via phase-transition modulation (~68 °C intrinsic, extendable to ~80 °C[76]), high temperature application is thermally constrained. In stark contrast, refractory-metal metasurfaces fabricated via fs-LMDW exhibit exceptional thermal resilience, sustaining cyclic operation at 300 °C (Fig. 4), surpassing PCMs in high-temperature robustness.

Fabrication complexity further distinguishes these approaches. Constructing a typical Al_2O_3/GST/ZnS/Au/Si encryption system demands multi-step processes: nanosecond/millisecond (ns/ms) laser irradiation for bump-structure lithography and phase modulation, thermal/electrical evaporation of stratified layers (150 nm Au, 850 nm ZnS, 25 nm GST, 30 nm Al_2O_3)[70]. Figure 6(d) entails the "4M" complexities for multi-layer Vis-IR information crosstalk-free GST-based metasurfaces: **M**ultiple fabrication steps (Al reflector, Cr IR emissivity modulator, a-GST deposition), **M**ultiple equipment (lasers for patterning), **M**ultiple masks (Vis/IR information and corresponding alignment), and **M**ultiple materials[62]. Thickness sensitivity also necessitates nanoscale precision. The adoption of nano-lithography[72,77] and noble metals (e.g., Au[71] and Ag[72]) also inflate cost and limit scalability. Conversely, fs-LMDW imposes minimal thickness constraints, allowing easy screening of the dual-band information-interference processing window, positioning it as a transformative platform to push forward the innovative manufacturing of cryptographic metasurfaces. The fs-LMDW technique on the basis of hierarchical structuring[24,25] also offers unparalleled advantages in operational simplicity, high writing velocity, flexible patterning, and material versatility, particularly advantageous for processing refractory metals/alloys and other hard-to-process materials[20,47,78,79].

Table 1 | Visible-infrared dual-band crosstalk-free information encryption techniques, details and their pros/cons.

Technique; key materials	Visible input	Infrared input	Pros	Cons	Ref
Magnetron sputtering; Si/Ge-Ge/PEI	Si-pattern selective coating	700 nm Ge pattern coding	IR-radiation direction control; visible-band colorful	Pattern mask needed for information input and color control	ref.[69]
Magnetron sputtering; GST/Cr/Al/Si	Laser induced a-to-c-GST phase transition	Cr-layer selective patterning	Wafer-sized patterning	Grey color confined; GST thickness dependent	ref.[62]
Ns/ms laser irradiation + thermal/electrical evaporation; Al_2O_3/GST/ZnS/Au/Si	Ns laser irradiation bump-structure patterning	Ms laser induced a-to-c GST phase transition	High resolution of information encoding (~0.6 μm, 4.23 × 10^4 dpi)	Complex layout, multiple equipment	ref.[70]
Magnetron sputtering + sample annealing; GST/Si multi-layer metasurface	Si-module (Si_{top}) with different film thicknesses	Emission control module [GST/Si] subjected to thermal annealing and Au pattern coating	Multi-color display modulation through IR-transparent films; IR-info erasability at 150 °C	High cost, pattern mask needed, low erasable temperature threshold	ref.[71]
UV-photolithography; selective laser irradiation and film deposition; GST-grating/Ag	Si_3N_4 patterned deposition (Ge layer for color enrichment)	c-GST nanograting and IR-info erasability at 150 °C	Multi-color display modulation through IR-transparent films	Pattern mask and multiple equipment needed, low erasable temperature	ref.[72]
PLD + self-assembly; W-doped VO_2 + PS microsphere	Self-assembled PS-microsphere layer	W-doped VO_2 films with W-atom percentages of 0, 0.8%, 1.7 %	Temperature-controlled stepwise IR information decryption	Pattern mask needed; overall Vis-color; loose PS microsphere layer	ref.[73]
Fs-LMDW; (Zr, Mo, W)	LIPSS nanostructuring in liquid (e.g., EG); grey/black	Micro/nanostructuring in air and composition alteration	Flexibility, convenience, erasability and rewritability; selective 300 °C HT-IR-decryption	Vis-band color-limited	This work

Note: Nanosecond/millisecond (ns/ms) laser; pulse laser deposition (PLD); polystyrene (PS); Polyetherimide (PEI); high temperature (HT)

Fs-LMDW achieves throughput metrics orders of magnitude superior to electron-beam lithography (EBL), which requires ≈11 min to fabricate a mere 1 mm^2 metasurface at 200 nm resolution[80]. Ref.[6] compares three cornerstone nanolithographies (EBL, focused ion beam (FIB), laser lithography) for metasurface fabrication, affirming the advantage of high-velocity laser-based methods. Our methodology extends this frontier by replacing ordered nanoscale patterning with randomly laser-driven hierarchical structuring, unlocking previously inaccessible design spaces for scalable fabrication of "structurally disordered to functionally ordered" photonic metasurfaces. During fs laser ablation, extreme temperatures (10^3 K order) and GPa-level shockwaves induces the m-ZrO_2 phase transition to metastable t-ZrO_2[47]. Although altering unit cell volume of ZrO_2[81] may theoretically generate internal stresses, experimental evidence demonstrates remarkable stability: subsurface m-ZrO_2→t-ZrO_2 transition in 3 mol% Y_2O_3 stabilized tetragonal zirconia polycrystals (3Y-TZP) resists ultrasonic washing[47]. Ultra-rapid thermal cycling inherent to fs laser ablation[47] is further enhanced in liquid media, facilitating crack-minimized t-ZrO_2 crystals' solidification[35]. Critically, structural evolution is confined to near-surface regions, inherently limiting volumetric strain and concomitant stress generation. Thus, it is deemed that fs-LMDW autonomously governs structural stability and structural morphology during laser-matter interactions, ensuring rewrite/erase-involving dual-band encryption/decryption functionalities.

4 Conclusions

This work demonstrates a novel methodology for multispectral all-in-one metasurface fabrication by fs laser maskless direct writing sequentially in air and EG environments, enabling visible information erasure and rewriting to deceive naked eyes and temperature-controlled stepwise decrypted display of IR-band encryption information. Complete decryption requires the temperature to reach 300 °C, effectively protecting the critical IR-encrypted information through harsh environment stimuli, a temperature can not be realized by phase transition materials for IR encryption. Decryption requires specific high temperatures, significantly enhance the security of information encryption. Visible information "SJTU" and IR information of a QR code that directs to a website are integratedly fabricated for conceptional validation. The erasability is due to the insufficient-oxidation black-coloration of visible information (i.e., introduction of a high density of oxygen vacancies), while the rewritability is aroused by removal of interfacial black NPs aggregates and LIPSS imprinting. There is a processing threshold of visible information input for crosstalk-free dual-band display and the erasable-to-rewritable capacities. Above this value, visible information displays together with the IR information, i.e., information crosstalking. One-time complete erasability of fs-LMDW fabricated metasurface is helpful to identify whether the encryption information has been decrypted. Through our finding, it is revealed that EG-nanostructuring and Air-micro/nanostructuring are the keys for rapid (200 mm/s) fs-LMDW fabrication of multispectral all-in-one metasurface, highly advantageous to PCM-based metasurfaces constrained by high design complexity, intricate fabrication processes, and dependency on predefined information encoding mask templates and essential adoption of multiple micro/nanofabrication techniques.

References

1. Zhu L, Xie WJ, Dong L et al. Metasurface-assisted chaotic cryptography platform for enhanced secure communication. *Laser Photonics Rev* **19**, e00955 (2025).
2. Fu R, Chen KX, Li ZL et al. Metasurface-based nanoprinting: principle, design and advances. *Opto-Electron Sci* **1**, 220011 (2022).
3. Zhu ZB, Li YF, Wang JF et al. Reconfigurable origami chiral response for holographic imaging and information encryption. *Opto-Electron Sci* **4**, 240026 (2025).
4. Liu TT, Han Z, Duan JY et al. Phase-change metasurfaces for dynamic image display and information encryption. *Phys Rev Appl* **18**, 044078 (2022).
5. Liu K, Lin ZY, Han B et al. Non-volatile dynamically switchable color display via chalcogenide stepwise cavity resonators. *Opto-Electron Adv* **7**, 230033 (2024).
6. Yang WH, Zhou JX, Tsai DP et al. Advanced manufacturing of dielectric meta-devices. *Photonics Insights* **3**, R04 (2024).
7. Kim G, Kim D, Lee J et al. Quasi-ordered plasmonic metasurfaces with unclonable stochastic scattering for secure authentication. *Nat Commun* **16**, 6269 (2025).
8. Yu ZP, Li HH, Zhao WN et al. High-security learning-based optical encryption assisted by disordered metasurface. *Nat Commun* **15**, 2607 (2024).
9. Lalanne P, Chen M, Rockstuhl C et al. Disordered optical metasurfaces: basics, properties, and applications. *Adv Opt Photonics* **17**, 45–112 (2025).
10. Kim D, Lee J, Kim G et al. Proton-assisted assembly of colloidal nanoparticles into wafer-scale monolayers in seconds. *Adv Mater* **36**, 2313299 (2024).
11. Fang Y, Hao H, Wang QS et al. Metasurface-generated spin-multiplexed & grafted perfect vector vortex beams for high-dimensional optical information encryption. *Laser Photonics Rev* **19**, 2402033 (2025).
12. Huang LY, Xu K, Yuan DD et al. Sub-wavelength patterned pulse laser lithography for efficient fabrication of large-area metasurfaces. *Nat Commun* **13**, 5823 (2022).
13. Lapidas V, Cherepakhin A, Storozhenko D et al. Surface coloring and plasmonic information encryption at 50000 dpi enabled by direct femtosecond laser printing. *Nano Lett* **24**, 12590–12596 (2024).
14. He GZ, Yan JF, Xie JW et al. Ultrafast laser processing of camouflaged metals by topography inherited multistep removal for information encryption. *Nano Res* **17**, 7242–7249 (2024).
15. Le VD, Eles B, Dalloz N et al. Understanding and exploiting the optical properties of laser-induced quasi-random plasmonic metasurfaces. *ACS Appl Opt Mater* **2**, 373–385 (2024).
16. Jiao SH, Zhao K, Jiang JH et al. Metasurface with all-optical tunability for spatially-resolved and multilevel thermal radiation. *Nanophotonics* **13**, 1645–1655 (2024).
17. Kim Y, Kim C, Lee M. Parallel laser printing of a thermal emission pattern in a phase-change thin film cavity for infrared camouflage and security. *Laser Photonics Rev* **16**, 2100545 (2022).

18. Yin SY, Guo Q, Liu SR et al. Three-dimensional multichannel waveguide grating filters. *Opto-Electron Sci* **3**, 240003 (2024).
19. Pavlov D, Zhizhchenko A, Pan L et al. Tuning collective plasmon resonances of femtosecond laser-printed metasurface. *Materials* **15**, 1834 (2022).
20. Liao JN, Zhang DS, Li ZG. Conceptional pure-tungsten metasurfaces based on femtosecond laser nanomanufacturing. *Engineering* **49**, 61–80 (2025).
21. Manshina AA, Tumkin II, Khairullina EM et al. The second laser revolution in chemistry: emerging laser technologies for precise fabrication of multifunctional nanomaterials and nanostructures. *Adv Funct Mater* **34**, 2405457 (2024).
22. Yuan YJ, Li X, Jiang L et al. Laser maskless fast patterning for multi-type microsupercapacitors. *Nat Commun* **14**, 3967 (2023).
23. Chen PC, Xu XY, Wang TX et al. Laser nanoprinting of 3D nonlinear holograms beyond 25000 pixels-per-inch for inter-wavelength-band information processing. *Nat Commun* **14**, 5523 (2023).
24. Liao JN, Li ZG, Zhang DS. Bionic femtosecond laser manufacturing for impressionistic camouflage infrared display. *Int J Extrem Manuf* **8**, 015010 (2026).
25. Liu RJ, Zhang DS, Li ZG. Femtosecond laser subtractive/additive-integrated biomimetic manufacturing for visible/infrared encryption and stimuli-responsive infrared decryption. *Int J Extrem Manuf* **7**, 045009 (2025).
26. Li YJ, Hu JT, Zeng YX et al. Recent progress on structural coloration. *Photonics Insights* **3**, R03 (2024).
27. Liu RJ, Zhang DS, Li ZG. Femtosecond laser induced simultaneous functional nanomaterial synthesis, in situ deposition and hierarchical LIPSS nanostructuring for tunable antireflectance and iridescence applications. *J Mater Sci Technol* **89**, 179–185 (2021).
28. Shih CY, Streubel R, Heberle J et al. Two mechanisms of nanoparticle generation in picosecond laser ablation in liquids: the origin of the bimodal size distribution. *Nanoscale* **10**, 6900–6910 (2018).
29. Zhai QX, Gong WQ, Yu MJ et al. Flexible fabrication of core/shell nanoparticles for tailored infrared emissivity on aluminum via femtosecond laser self-deposition. *Opt Lett* **49**, 5192–5195 (2024).
30. Tsibidis GD, Fotakis C, Stratakis E. From ripples to spikes: a hydrodynamical mechanism to interpret femtosecond laser-induced self-assembled structures. *Phys Rev B* **92**, 041405 (2015).
31. Kirner SV, Hermens U, Mimidis A et al. Mimicking bug-like surface structures and their fluid transport produced by ultrashort laser pulse irradiation of steel. *Appl Phys A* **123**, 754 (2017).
32. Ahmmed KMT, Grambow C, Kietzig AM. Fabrication of micro/nano structures on metals by femtosecond laser micromachining. *Micromachines* **5**, 1219–1253 (2014).
33. Sedao X, Shugaev MV, Wu CP et al. Growth twinning and generation of high-frequency surface nanostructures in ultrafast laser-induced transient melting and resolidification. *ACS Nano* **10**, 6995–7007 (2016).
34. Zhang DS, Ranjan B, Tanaka T et al. Carbonized hybrid micro/nanostructured metasurfaces produced by femtosecond laser ablation in organic solvents for biomimetic antireflective surfaces. *ACS Appl Nano Mater* **3**, 1855–1871 (2020).
35. Xu LR, Tao JC, Li TH et al. Under liquid femtosecond laser sintering of highly reflective 3Y-TZP refractory ceramics assisted by multi-functional Fe_3O_4 dopants. *J Mater Sci Technol* **247**, 64–80 (2026).
36. Li TH, Tang RJX, Xu LR et al. Femtosecond laser ablation of high-entropy ceramics $RE_2(Ce_{0.2}Zr_{0.2}Hf_{0.2}Sn_{0.2}Ti_{0.2})_2O_7$ (RE = Sm, Eu, Er) in liquid for colloid synthesis. *J Phys Chem C* **129**, 3707–3720 (2025).
37. Zhang DS, Ranjan B, Tanaka T et al. Underwater persistent bubble-assisted femtosecond laser ablation for hierarchical micro/nanostructuring. *Int J Extrem Manuf* **2**, 015001 (2020).
38. Zhou HB, Yao PP, Gong TM et al. Effects of ZrO_2 crystal structure on the tribological properties of copper metal matrix composites. *Tribol Int* **138**, 380–391 (2019).
39. Fromme T, Reichenberger S, Tibbetts KM et al. Laser synthesis of nanoparticles in organic solvents-products, reactions, and perspectives. *Beilstein J Nanotechnol* **15**, 638–663 (2024).
40. Streubel R, Barcikowski S, Gökce B. Continuous multigram nanoparticle synthesis by high-power, high-repetition-rate ultrafast laser ablation in liquids. *Opt Lett* **41**, 1486–1489 (2016).
41. Witke K, Österle W, Skopp A et al. Raman microprobe spectroscopy and transmission electron microscopy of thermal sprayed ZrO_2 coatings before and after rub testing of outer air seals. *J Raman Spectrosc* **32**, 1008–1014 (2001).
42. Li C, Li MJ. UV Raman spectroscopic study on the phase transformation of ZrO_2, Y_2O_3-ZrO_2 and SO_4^{2-}/ZrO_2. *J Raman Spectrosc* **33**, 301–308 (2002).
43. Cangueiro LT, Cavaleiro AJ, Morgiel J et al. Mechanisms of the formation of low spatial frequency LIPSS on Ni/ Ti reactive multilayers. *J Phys D Appl Phys* **49**, 365103 (2016).
44. Piatkowski P, Ali A, Alawadhi H et al. Simultaneous carburization, oxidation, and nitridation of titanium surface using ablation by femtosecond laser in n-heptane. *Adv Eng Mater* **25**, 2201361 (2023).
45. Ammar MR, Galy N, Rouzaud JN et al. Characterizing various types of defects in nuclear graphite using Raman scattering: Heat treatment, ion irradiation and polishing. *Carbon* **95**, 364–373 (2015).
46. Yuan RC, Guo YW, Gurgan I et al. Raman spectroscopy analysis of disordered and amorphous carbon materials: a review of empirical correlations. *Carbon* **238**, 120214 (2025).
47. Xu LR, Tao JC, Li ZG et al. Femtosecond laser ultrafast photothermal exsolution. *Int J Extrem Manuf* **6**, 055002 (2024).
48. Prybyla JA, Heinz TF, Misewich JA et al. Desorption induced by femtosecond laser pulses. *Phys Rev Lett* **64**, 1537–1540 (1990).
49. Glover TE. Hydrodynamics of particle formation following femtosecond laser ablation. *J Opt Soc Am B* **20**, 125–131 (2003).
50. Garvie RC. The occurrence of metastable tetragonal zirconia as a crystallite size effect. *J Phys Chem* **69**, 1238–1243 (1965).
51. Zhang DS, Gökce B, Barcikowski S. Laser synthesis and processing of colloids: fundamentals and applications. *Chem Rev* **117**, 3990–4103 (2017).
52. Segovia P, Wong A, Santillan R et al. Multi-phase titanium oxide LIPSS formation under fs laser irradiation on titanium thin films in ambient air. *Opt Mater Express* **11**, 2892–2906 (2021).
53. Fan LS, Wu L, Wang YJ et al. Femtosecond laser induced oxygen vacancies in CeO_2 with filament-type resistive switching memory. *Appl Surf Sci* **690**, 162555 (2025).
54. Amendola V, Amans D, Ishikawa Y et al. Room-temperature laser synthesis in liquid of oxide, metal-oxide core-shells, and doped oxide nanoparticles. *Chem Eur J* **26**, 9206–9242 (2020).
55. Chen XD, Meng C, Wang Y et al. Laser-synthesized rutile TiO_2 with abundant oxygen vacancies for enhanced solar water evaporation. *ACS Sustainable Chem Eng* **8**, 1095–1101 (2020).
56. Qi JY, Liu XQ, Liu ZJ et al. Ultrawide spectrum metallic plane blackbody with extremely high absorption from 0.2 to 25 μm. *Adv Sci* **12**, 2411448 (2025).
57. Andrews SS. Thermal radiation. In Andrews SS. *Light and Waves: A Conceptual Exploration of Physics* 307–328 (Springer, Cham, 2023).
58. Deng ZC, Su YR, Qin W et al. Nanostructured Ge/ZnS films for multispectral camouflage with low visibility and low thermal emission. *ACS Appl Nano Mater* **5**, 5119–5127 (2022).
59. Ding YX, Wang QC. Preparation and research of new black zirconia ceramics. *Sci Rep* **14**, 3197 (2024).
60. Khojier K, Savaloni H, Jafari F. Structural, electrical, and decorative properties of sputtered zirconium thin films during post-annealing process. *J Theor Appl Phys* **7**, 55 (2013).
61. Zhang DS, Liu RJ, Li ZG. Irregular LIPSS produced on metals by

single linearly polarized femtosecond laser. *Int J Extrem Manuf* **4**, 015102 (2022).
62. Kim C, Kim Y, Kang D et al. Laser-printed emissive metasurface as an anticounterfeiting platform. *Laser Photonics Rev* **16**, 2200215 (2022).
63. Zhang DS, Li ZG, Sugioka K. Laser ablation in liquids for nanomaterial synthesis: diversities of targets and liquids. *J Phys Photonics* **3**, 042002 (2021).
64. Zacharatos F, Duderstadt M, Almpanis E et al. Laser printing of Au nanoparticles with sub-micron resolution for the fabrication of monochromatic reflectors on stretchable substrates. *Opt Laser Technol* **135**, 106660 (2021).
65. Hu YX, Zhou Y, Luo GH et al. Femtosecond laser-induced nanoparticle implantation into flexible substrate for sensitive and reusable microfluidics SERS detection. *Int J Extrem Manuf* **6**, 045005 (2024).
66. Ng RJH, Krishnan RV, Dong ZG et al. Micro-tags for art: covert visible and infrared images using gap plasmons in native aluminum oxide. *Opt Mater Express* **9**, 788–801 (2019).
67. Lee JH, Kim YJ, Yoo YJ et al. Colored, covert infrared display through hybrid planar-plasmonic cavities. *Adv Opt Mater* **9**, 2100429 (2021).
68. Kang D, Kim Y, Lee M. Multispectral imaging with a planar cavity-type metasurface for optical security. *ACS Appl Mater Interfaces* **15**, 29577–29585 (2023).
69. Ying YB, Yu JB, Qin B et al. Directional thermal emission covering two atmospheric windows. *Laser Photonics Rev* **17**, 2300407 (2023).
70. Xu ZQ, Luo H, Zhu HZ et al. Nonvolatile optically reconfigurable radiative metasurface with visible tunability for anticounterfeiting. *Nano Lett* **21**, 5269–5276 (2021).
71. Huo LX, Li Z, Ye XY et al. Wavelength-selective emission of $Ge_2Sb_2Te_5$/Si multilayer structures for dynamic adaptive camouflage and optical security. *Small* **21**, 2503932 (2025).
72. Li Z, Huo LX, Ye XY et al. Phase-change grating multispectral camouflage system for security applications: dynamic regulation and information encryption. *Laser Photonics Rev* e01651 (2025).
73. Wang J, Wang MR, Xie QD et al. Multilevel information encryption mediated by reconfigurable thermal emission in smart bilayer material. *Laser Photonics Rev* **18**, 2301106 (2024).
74. Kushchenko OM, Gets DS, Rybin MV et al. All optically switchable active photonics based on the halide perovskite GST platform. *Laser Photonics Rev* **17**, 2200836 (2023).
75. Wei H, Gu JX, Ren FF et al. Kirigami-inspired reconfigurable thermal mimetic device. *Laser Photonics Rev* **16**, 2200383 (2022).
76. Chen FQ, Liu Y, Liu XJ et al. Multistate spectral-tunable manipulation of mid-infrared emissivity using Sb_2S_3/GST/VO_2. *Appl Phys Lett* **122**, 191702 (2023).
77. Zhang F, Guo YH, Pu MB et al. Meta-optics empowered vector visual cryptography for high security and rapid decryption. *Nat Commun* **14**, 1946 (2023).
78. Obata K, Kawabata S, Hanada Y et al. High performance micromachining of sapphire by laser induced plasma assisted ablation (LIPAA) using GHz burst mode femtosecond pulses. *Opto-Electron Sci* **3**, 230053 (2024).
79. Wang HJ, Zhao XY, Xie ZC et al. Bioinspired directional structures for inhibiting wetting on super-melt-philic surfaces above 1200 °C. *Int J Extrem Manuf* **6**, 045503 (2024).
80. Sin Tan Y, Wang H, Wang HT et al. High-throughput fabrication of large-scale metasurfaces using electron-beam lithography with SU-8 gratings for multilevel security printing. *Photonics Res* **11**, B103–B110 (2023).
81. Ohtaka O, Fukui H, Kunisada T et al. Phase relations and equations of state of ZrO_2 under high temperature and high pressure. *Phys Rev B* **63**, 174108 (2001).

Acknowledgements

We are grateful for financial supports from the Instrumental Analysis Center of SJTU. We gratefully acknowledge the financial support received from the Shanghai Pujiang Program (23PJ1406500).

Author contributions

Conception: H. Jiang., D. Zhang; Original writing: H. Jiang., D. Zhang; Supervision: D. Zhang, Z. Li; All the authors read and approved the final manuscript.

Competing interests

The authors declare that they have no known competing financial interests or personal relationships that could have appeared to influence the work reported in this paper.

Supplementary information

Supplementary information for this paper is available at
https://doi.org/10.29026/oea.2026.250303

Open Access This article is licensed under a Creative Commons Attribution 4.0 International License, which permits use, sharing, adaptation, distribution and reproduction in any medium or format, as long as you give appropriate credit to the original author(s) and the source, provide a link to the Creative Commons license, and indicate if changes were made. To view a copy of this license, visit
http://creativecommons.org/licenses/by/4.0/
©The Author(s) 2026.
Published by Editorial Office of *Opto-Electronic Advance*, Institute of Optics and Electronics, Chinese Academy of Sciences.

Opto-Electronic Journals Group
www.oejournal.org
Scan for Article PDF